Integrating Materials and Manufacturing Innovation (2019) 8:82–94
https://doi.org/10.1007/s40192-019-00127-6

THEMATIC SECTION: 5TH WORLD CONGRESS ON INTEGRATED COMPUTATIONAL MATERIALS ENGINEERING

Computational Design of Functionally Graded Materials from Sintered Powders

Tesfaye T. Molla [1] · J. Z. Liu [1] · G. B. Schaffer [1]

Received: 1 January 2019 / Accepted: 19 February 2019 / Published online: 4 March 2019

Abstract

A new computational method is presented for the efficient design of alloy systems in functionally graded materials (FGMs), optimized for manufacturability (sintering) as well as performance. The design methodology uses a multi-objective genetic algorithm (GA) integrated with computational thermodynamics and physics-based predictive models to optimize the composition of each alloy in the FGM. Thermodynamic modeling, using the CALPHAD method, is used to establish microstructural constraints and calculate the effective diffusivity in each alloy of the FGM. Physics-based predictive models are used to estimate performance properties. The model is verified by comparing results with data from the literature. A design exercise is also presented for an FGM that combines a ferritic and an austenitic stainless steel to demonstrate the capability of the methodology. It is shown that the mismatch in sintering rate between the two alloys, which causes processing defects during co-sintering, can be minimized while the solution hardening and corrosion resistance in the austenitic alloy can be optimized by independently controlling the composition of both alloys, the initial particle sizes and the sintering temperature.

Keywords Integrated Computational Materials Engineering (ICME) · Functionally graded materials · Design of alloys · Sintering

Introduction

Progress in the development of Integrated Computational Materials Engineering (ICME) offers new capabilities in dealing with the challenge of material design, which is typically a multi-dimensional optimization problem requiring many thousands of experiments [1, 2]. The design problem can get explosively complicated when it is necessary to control both composition and the processing parameters/conditions while simultaneously optimizing for two or more properties in multi-component systems, such as those found in functionally graded materials (FGMs). One solution is a top-down, performance-driven reduced order meta-model that incorporates a spectrum of process conditions and material properties and is computationally low-cost and sufficiently accurate to support engineering decision-making [3, 4].

Recently, we developed an ICME framework for the design of sintered alloys using such a reduced order meta-model [5]. The design method follows a material systems approach that integrates processing, structure, and property relations. It includes a multi-objective genetic algorithm (GA) to optimize alloy composition with the aim of improving the sintering as well as performance-related properties. The GA is coupled with computational thermodynamics and predictive analytical property models. Thermodynamic simulations, based on the CALPHAD method, are used to establish constraints through phase stability at equilibrium and calculate the diffusivity that determines the sintering behavior of the alloy. This enables the design of new alloys which are simultaneously optimized for improved sinterability, yield strength, corrosion resistance, and cost.

Here, we extend this model to the design of stepwise, layered FGMs fabricated through a multi-component metal injection molding route in which two-color plastic injection molding (2C-MIM) technology is used to make a bi-material structure [6–12]. The co-sintering of two-metal systems is challenging because differences in sintering rate between the individual metals generate internal stresses causing distortion and interface cracking, while diffusion of alloying elements across the boundary can result in deleterious phases close to the

✉ Tesfaye T. Molla
tesfaye.molla@unimelb.edu.au

[1] Department of Mechanical Engineering, The University of Melbourne, Parkville, Victoria 3010, Australia

interface region [13]. It is therefore necessary to minimize the sintering mismatch between the two layers while also maximizing the desirable properties in each layer. Because these factors are all interdependent, a conventional, experimentally based design campaign requires thousands of experiments over a very long time and at high cost making the insertion of new FGMs into advanced products and systems very difficult.

To demonstrate the design methodology, we consider a FGM system that combines ferromagnetic and non-magnetic stainless steel alloys made by two-color injection molding of metal powders. During the design, a GA is used to alter the composition of each alloy in the two domains of the FGM to minimize the mismatch in their sintering rates, which is the primary cause of process defects. Simultaneously, the composition of the austenitic stainless steel alloy is also optimized to increase the hardness and corrosion resistance. The average powder particle sizes and the sintering temperature are also included in the optimization. The design methodology is implemented using MATLAB™ coupled with Thermo-Calc (TC), a thermodynamic modeling software, through the TC-MATLAB interface. We verify the methodology by comparing model predictions with experimental results from the literature.

Co-sintering of Multi-layers

This section reviews the constitutive behavior of powder compacts during solid-state sintering and the models used to predict shape distortion during co-sintering of multi-materials. Material system and design objectives for sintered FGMs are also developed.

Constitutive Behaviors of Sintering Bodies

The macrostructural behavior of a porous body during sintering can be analyzed using the continuum theory of sintering which has been widely applied to describe the sintering behavior of multi-layered powder compacts or systems [14–17]. A porous body at sintering temperature is assumed to have a linear viscous behavior, where the total strain rate, $\dot{\varepsilon}_{ij} = d\varepsilon_{ij}/dt$, is proportional to the equivalent stress, σ_{ij}, in the porous body [18] as:

$$\dot{\varepsilon}_{ij} = \frac{\sigma'_{ij}}{2G'} + \frac{(\sigma_m - \sigma_s)\delta_{ij}}{3K'} \tag{1}$$

where $\sigma'_{ij}, \sigma_m, and\ \sigma_s$ are the deviatoric component of the equivalent stress, the hydrostatic mean, and the inherent sintering stresses; G' and K' are the effective shear and bulk viscosities of the sintering body; and δ_{ij} is the Kronecker delta. The driving force for sintering is the sintering stress, σ_s, which is a function of the surface energy per unit area, γ_s, as [18]:

$$\sigma_s = \frac{3}{2}\frac{\gamma_s}{G}(1-\theta)^2 \tag{2}$$

where G is the particle size and θ is the amount of porosity. Similarly, the effective shear and bulk viscosities of the porous powder system are functions of temperature, particle size, and amount of porosity during the sintering cycle. From Eq. (1), the axial shrinkage strain rate in a freely sintering body, i.e., with no external as well as internal stress affecting the shrinkage behavior, can be given by:

$$\dot{\varepsilon}_{ij} = -\frac{\sigma_s \delta_{ij}}{3K'} \tag{3}$$

Stress and Shape Distortion During Co-sintering of Multi-layers

During sintering of an asymmetric bi-layer structure, the difference in shrinkage rate between the two layers generates an internal in-plane force, N and bending moment M as shown in Fig. 1. The structure relaxes the internal stress (i.e., caused by the force and bending moment) by warping, resulting in distortion of the sample. The internal stresses vary across the thickness of the individual layers and affect the shrinkage rate depending on the direction of the stress in each layer. For the geometry shown in Fig. 1, the stress normal to the interface between the two layers is very small compared to the in-plane stresses. The relative mismatch in shrinkage rate thus generates a bi-axial stress in the sample during sintering.

By applying the linear viscous version of the continuum theory of sintering, Cai et al. [14], Kanters et al. [15], and Frandsen et al. [16] have shown that the curvature, k, of the distorted sample evolves as:

$$k = \frac{6nm(m+1)\left(\dot{\varepsilon}_2^f - \dot{\varepsilon}_1^f\right)}{n^2m^4 + n(4m^3 + 6m^2 + 4m) + 1} \tag{4}$$

Here, $\dot{\varepsilon}_i^f$ (for $i = 1$ or 2) represents the free body shrinkage rate of the corresponding layer in the bi-layer, and the factors m and n are given by:

$$m = \frac{h_1}{h_2}; \text{and}\ \ n = \frac{\eta_1}{\eta_2} \tag{5}$$

where h_i and η_i (for $i = 1$ or 2) represent the initial thickness and the effective uniaxial viscosity for each of the layers.

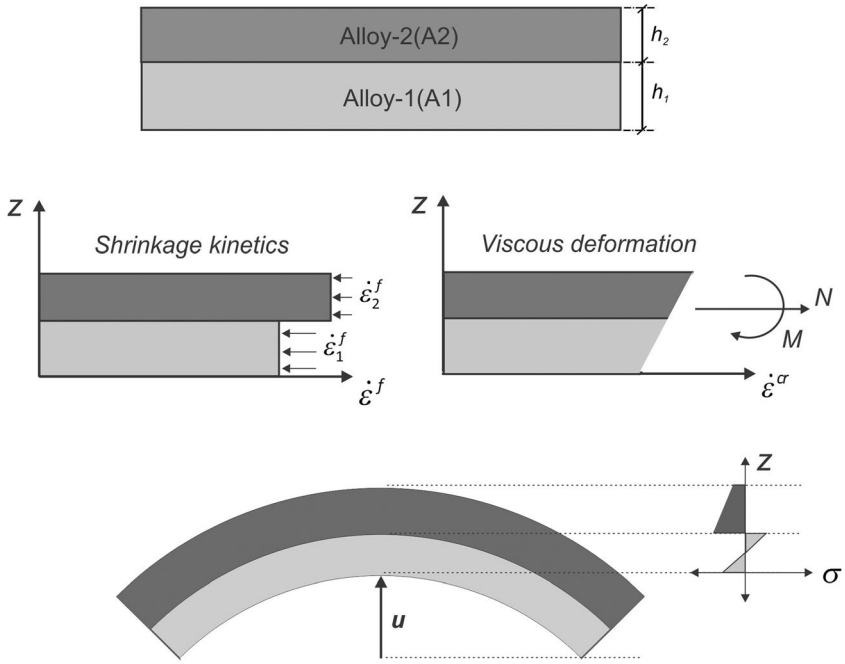

Fig. 1 Schematic diagram of a bilayer showing stress distributions and deformation during co-sintering (u represents the distortion with respect to the surface)

Equation (4) shows that the curvature development in the asymmetric bilayer system depends on:

1. The mismatch in free shrinkage rate between the layers;
2. The ratio of the effective uniaxial viscosity of the layers; and
3. The ratio of initial thickness of the layers.

For an isothermal sintering, the ratio of the effective uniaxial viscosities between the two layers can also be related to the ratio of their shrinkage rates [16].

Design Objectives for a Stepwise FGM Structure

Consider a discretely graded or stepwise FGM system involving two alloys (A1 and A2) as shown schematically in Fig. 2. The design optimization aims to enhance the functional properties of both alloys while simultaneously eliminating distortion during fabrication by reducing the mismatch in sintering rates between the two alloys.

Fig. 2 Schematic of an FGM system involving two metallic alloys with equal thickness

It is considered that the FGM involves soft magnetic stainless steel based on ferritic (A1) and corrosion-resistant stainless steel based on austenitic (A2) alloys, which are processed by 2C-MIM. We further assume that:

1. The powder compact in each of the alloys is made from a uniform dispersion of monosized spherical particles. This is typical for a MIM feedstock and avoids the need to account for factors related to powder compacts with different particle sizes and shapes.
2. The two alloys in the FGM are considered to have equal initial thicknesses, i.e., $h_1 = h_2$. This consideration removes the effect of thickness ratio on the development of stress or curvature during co-sintering of the two alloys.
3. The FGM system is produced under isothermal sintering condition.

Considering Eq. (4), the curvature evolution during co-sintering of the FGM will primarily be affected by the mismatch in sintering/shrinkage rate between the alloys, i.e., $\dot{\varepsilon}_2^f - \dot{\varepsilon}_1^f$. Following the material systems design chart suggested in Molla et al. [5] for stainless steel alloys produced by MIM, the shrinkage rate in each alloy is a function of the green density (initial porosity), particle size, and the effective self-diffusion coefficient of the multi-component alloy. As shown by Molla et al. [5], an alloy can be designed for sintering by optimizing the compositions of alloying elements. It is therefore possible to design alloys A1 and A2 in a

way that minimizes the sintering rate mismatch to realize defect-free co-sintering of the FGM. For illustrative purposes, the design objectives that we consider for the FGM system in this case are:

1) Minimize the mismatch in shrinkage rate between the two alloys;
2) Enhance the corrosion resistance of the ferritic alloy (Alloy-1); and
3) Enhance the hardness and corrosion resistance in the austenitic alloy (Alloy-2)

Computational Design Framework

Similar to the approach discussed in Molla et al. [5], the design framework involves a microstructural criterion for each alloy, and the multi-objective optimization for the compositions of each of the alloys that make up the FGM system. The optimization is performed using a genetic algorithm which evaluates candidate alloys based on feedback from (1) computational thermodynamics for microstructural constraints and the effective self-diffusivity of each alloy at a given sintering temperature and (2) predictive physics-based models for mechanical and corrosion resistance properties.

Computational Thermodynamics

Phase fraction and other important thermodynamic parameters at the sintering temperature for each of the alloys with a known mix of composition can be calculated using Thermo-Calc, a commercial software based on the CALPHAD method [19]. By appending an appropriate mobility database to the thermodynamic calculations, it is also possible to determine the effective kinetic parameters for each of the alloys. Thus, the thermodynamic database for iron alloys, TCFE9, was coupled to the mobility database, MOBFE4, and results were accessed through MATLAB using the TC-MATLAB interface, as described in Molla et al. [5].

Microstructural Stability

The stability of the microstructures for each of the alloys in the FGM system must be secured. In this regard, separate microstructural criterion are defined for each alloy. For the ferritic stainless steel (Alloy-1), only microstructures made of a ferritic (α) matrix are allowed. Similarly, for the austenitic stainless steel (Alloy-2), only microstructures consisting of an austenitic (Υ) matrix are considered. Alloys containing other phases at the sintering temperature receive a larger numerical penalty on the fitness criterion so that they have less chance of being selected.

Modeling the Effective Self-diffusivity of Alloys

Modeling the sintering rate of an alloy powder compact (green body) requires determination of the effective diffusion coefficient of the multi-component alloy at the sintering temperature. Because the green bodies of each of the alloys in the FGM are assumed to be made from spherical powders with uniform size and spatial distribution, it is only necessary to consider the effective self-diffusivity of the alloys. We further assume that the diffusion coefficient of the base or dominant element (Fe) in the alloy system at equilibrium is the effective diffusion coefficient of the alloy.

Thermo-Calc is used to calculate the effective tracer-diffusivities, D_{α}^{tr} or D_{γ}^{tr}, of each alloy in the FGM with the corresponding α or Υ phases at the sintering temperature. The tracer diffusion coefficient is close to but not identical to the self-diffusion coefficient. However, the effective self-diffusion coefficient, D_{Fe}^{s}, is often related to the tracer diffusion coefficient by a constant [20]. For the austenitic stainless steel alloy, this relationship can be given by:

$$D_{\gamma}^{s} = D_{\gamma}^{tr}/C_1 \tag{6}$$

Similarly, for the ferritic stainless steel alloy, the effective self-diffusion coefficient can be calculated considering the fraction of a stable phase, i.e., bcc (α), at the sintering temperature as:

$$D_{\alpha}^{s} = D_{\alpha}^{tr}/C_2 \tag{7}$$

Here, C_1 is a correlation factor varying between 0.6 to 1.0 depending on the crystal structure and the diffusion mechanism. For diffusion dominated by the vacancy mechanism in a face-centered and body-centered cubic lattices, the correlation factors can be assumed to be $C_1 = 0.78$ and $C_2 = 0.73$ [20].

Predictive Models

Modeling the Free Sintering Rate

Once the effective self-diffusion coefficient of an alloy is determined using computational thermodynamics, the sintering rate of the alloy's powder compact can be modeled using solid-state sintering models. A powder compact during MIM is often assumed to be governed

by lattice diffusion that can be modeled by considering the modified version of the Nabarro-Herring creep equation [21]. Thus, the linear shrinkage or strain rate, $\dot{\varepsilon}_L$, during sintering at isothermal temperature, T, is given by:

$$\dot{\varepsilon}_L = \frac{\dot{\rho}}{3\rho} = \frac{40}{3}\left(\frac{D^s \Omega}{G^2 kT}\right) D_F \tag{8}$$

where ρ represents the relative density and $\dot{\rho} = d\rho/dt$; D^s is the self-diffusion coefficient; Ω is the atomic volume; G is the particle size; k is the Boltzmann constant; and D_F is the driving stress for sintering. During free sintering, the only driving force for sintering is the intrinsic sintering stress, σ_s, and hence $D_F = \sigma_s$. By combining Eqs. (2) and (8), the linear shrinkage rate of the powder compact can be given by:

$$\dot{\varepsilon}_L = 20\left(\frac{D^s \Omega \gamma_s}{G^3 kT}\right)(1-\theta)^2 \tag{9}$$

Considering conservation of mass, the volumetric shrinkage/strain rate, $\dot{\varepsilon}_v$, of a powder compact during sintering can also be expressed in terms of porosity, θ, where, $\theta = 1 - \rho$, as [18]:

$$\dot{\varepsilon}_v = 3\dot{\varepsilon}_L = \frac{\dot{\theta}}{1-\theta} \tag{10}$$

Coarsening of particles during sintering is considered using an inverse square root function usually used for metallic powders involving a grain growth coefficient k' and an initial particle size, G_0, as [22]:

$$G = \frac{k' G_0}{(1-\rho)^{1/2}} \tag{11}$$

Modeling Solution Hardening

The analytical model proposed by Walbruhl et al. [23] provides a practical formalism for modeling solid solution hardening in the context of computational design of multi-component alloys. It was used by Molla et al. [5] to predict solution hardening of austenitic stainless steel alloys. This study also uses the model suggested in [23] to calculate solid solution hardening of the austenitic stainless steel alloy (A2) in the FGM system. Details of the methodology to determine parameters for the model can be found in Molla et al. [5].

Modeling Pitting Corrosion Resistance

The pitting corrosion resistance in a multi-component alloy is mainly dependent on the equivalent chromium composition. This is often represented by a factor called the pitting resistance equivalent, PRE, which represents the capacity of an alloy to resist pitting [24]:

$$PRE = \%Cr + 3\%Mo + 16\%N \tag{12}$$

Multi-objective Optimization Using GA

Computational thermodynamics as well as physics-based models are integrated through a GA that generates and improves candidate FGM systems using valid alloys as per the microstructural constraints in each domain. The improvement of candidate FGMs is performed based on the design objectives discussed in "Design Objectives for a Stepwise FGM Structure." These are (1) minimize the mismatch in sintering rates, $\Delta\dot{\varepsilon}$ between the two alloys of the FGM, i.e., A2 and A1; (2) maximize the change in strength due to solid solution hardening ($\Delta\sigma_{sss}$) in A2; and (3) maximize the pitting corrosion resistance (PRE) in both A1 and A2. Note that minimization of sintering rate mismatch between the two alloys requires predicting the linear shrinkage rate in each alloy. As shown in Eq. (9), the difference in free shrinkage rate between the alloys during sintering at a given temperature is primarily proportional to the difference in the ratio of the effective self-diffusion coefficient to the cube of particle size, i.e., $\Delta\dot{\varepsilon} \sim \Delta(D^s/G^3)$. Note here that the effective diffusion coefficient, D^s, depends on the chemical composition of the alloy whereas particle size, G, is proportional to the initial particle size of the powder compact. Thus, the design of a stepwise FGM for defect-free co-sintering can be optimized by controlling composition and processing parameters (particularly the initial particle size) in each of the alloys constituting the FGM.

Thus, a stepwise FGM candidate can be defined by considering two alloys (A1 and A2) with their respective chemical compositions and initial particle sizes. In other words, the chemical composition and initial particle sizes for A1 and A2 are the decision variables in the multi-objective optimization. The first design objective, i.e., minimizing mismatch in sintering rates between the two alloys in the FGM, can be achieved by calculating the ratio, D^s/G^3, for each alloy and then minimizing the difference. The other design goals can be optimized after calculation of the objective values by using the predictive models discussed in "Modeling Solution Hardening" and "Modeling Pitting Corrosion Resistance."

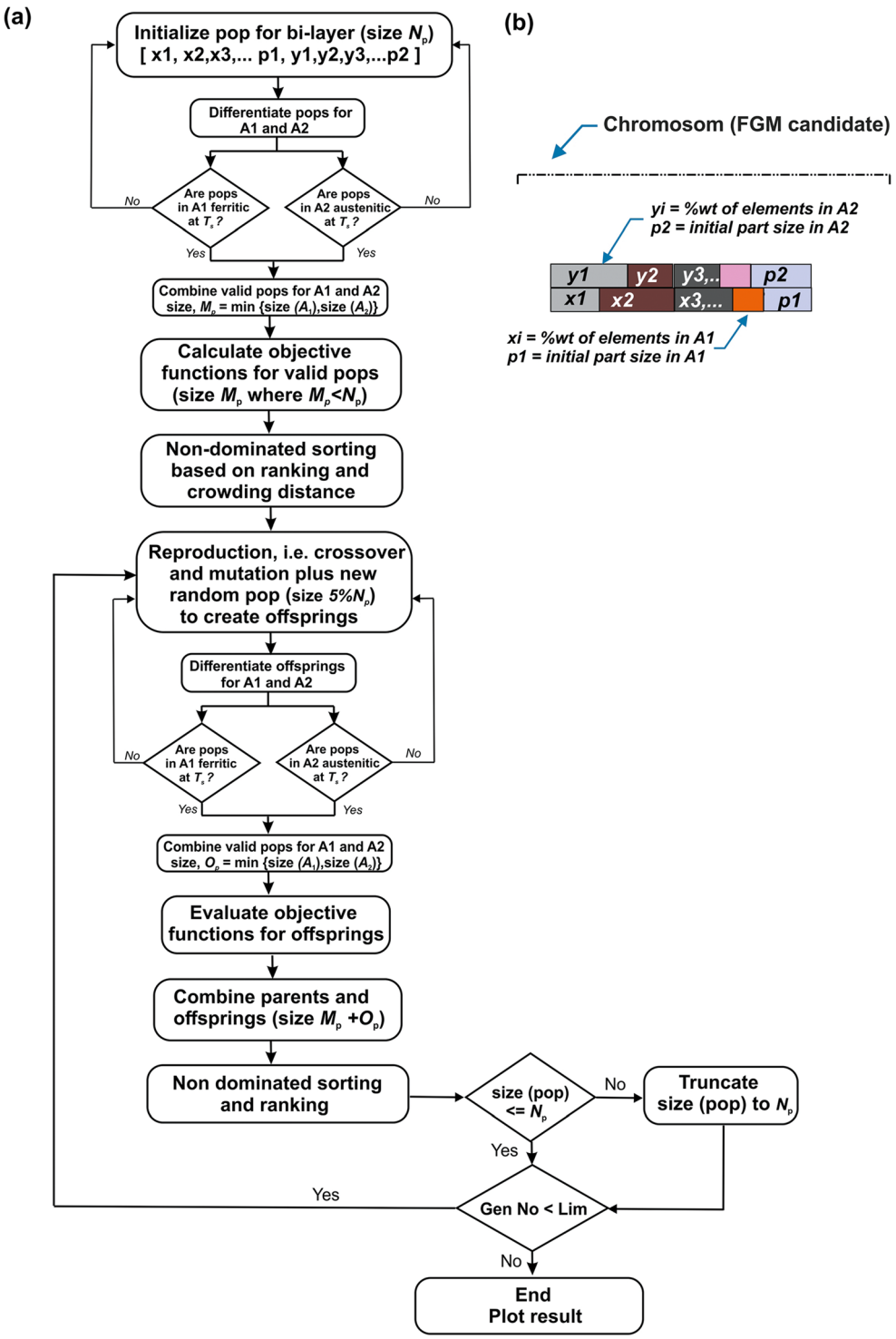

Fig. 3 **a** Flow chart of the NSGA-II. **b** Example of an individual chromosome for a FGM candidate

The non-dominated sorting genetic algorithm (NSGA-II) [25] is used to carry out the multi-objective optimization task. The NSGA-II provides a set of non-dominated optimal solutions for each alloy in the FGM structure, and this set of solutions is known as a Pareto-set. Figure 3 a shows the flow chart for the optimization algorithm developed in this study. In NSGA-II, the FGM structure is considered a chromosome having two sets of genes corresponding to each alloy in the FGM representing the percentage by weight of alloying elements and the initial particle sizes, see Fig. 3 b. The initialization of chromosomes, which are encoded using binary numbers, is performed by numeric randomization using a predefined minimum and maximum bound for

each of the genes and a tolerance of 0.1. Values of the genes in each chromosome are then decoded for evaluation of the objective functions. Further details on the application of NSGA-II for multi-objective optimization can be found in [25]. The population of these chromosomes evolves through varying the values of the genes according to their fitness to the objective function.

The NSGA-II employed in this study involves the following steps, see Fig. 3 a:

1. An initial set of N_p chromosomes (FGM population) consisting of the concentration (wt%) of elements (x_i and y_i) and the initial particle sizes (p_1 and p_2) for the two alloys (A1 and A2) are generated randomly within a predefined range (bound) for each of the decision variables (i.e., wt% of elements and particle sizes).
2. The composition (wt%) for each of the alloys is extracted from the main chromosome, and the alloy is tested against the microstructural constraint defined for the respective domain in the FGM. This is performed by calculation of the phase fraction using the composition of each alloy at the sintering temperature and pressure using Thermo-Calc. This step tests the individual alloys for the criterion discussed in "Microstructural Stability." If the number of either of the alloys (i.e., A1 with fully ferritic or A2 with fully austenitic phases) is less than 100, a new set of initial populations are generated once again by going back to step 1. This ensures that there are enough individuals for reproduction during the optimization.
3. From the entire population, M_p candidates ($M_p < N_p$) with valid microstructures for both alloys (i.e., fully ferritic A1 and fully austenitic phase A2) are selected and combined to form a new set of FGM candidates.
4. In each of the FGM candidates, the following objective values are calculated: (1) the effective self-diffusion coefficient (D^s) for both A1 and A2, (2) change in strength due to solid solution hardening ($\Delta\sigma_{sss}$) for A2, and (3) pitting corrosion resistance equivalent (*PRE*) for A1 and A2. These calculations are performed using the property module of Thermo-Calc and the predictive models discussed in "Computational Thermodynamics" and "Predictive Models," respectively.
5. Using the initial particle size for each alloy in the FGM, the first objective value, i.e., the difference in the ratio of the effective self-diffusion coefficient to the cube of particle size, $\Delta(D^s/G^3)$, is determined for A1/A2 in each of the FGM candidates.
6. Non-dominated sorting of the M_p candidates is then performed using the three objective values based on ranking and calculations of crowding distance as per the algorithm in NSGA-II [25].
7. Reproduction by crossover and mutation is then performed on the set of individuals (population) obtained from step 3 to produce offspring (children).
8. The microstructural stability of A1 and A2 for the offspring population is also tested. Those that have valid microstructures for each domain of the FGM at the sintering temperature are combined to form another FGM candidate of offspring, followed by evaluation of their objective values as in steps 4 and 5.
9. Offspring population of FGMs are then combined with the parents and sorted according to their ranking and crowding distance.
10. To diversify the pool of candidates after every iteration, a new set of randomly generated individuals, about 5% of the population after reproduction, is added in step 7. This enhances the search performance by diversifying the solution space and helps to avoid convergence or trapping to local optima or extrema.
11. The reproduction continues until the number of generations (Gen no) reaches a predefined limit (Lim), which is determined by the improvement in the objective values with the number of iterations.

Application of the Design Methodology

Here, we first validate the model by comparing with data from the literature. Design inputs, i.e., bounds for the composition of alloying elements and initial particle sizes for the stepwise FGM system defined in "Design Objectives for a Stepwise FGM Structure" are also presented, followed by the results and discussion.

Model Validation

The capability of the sintering model as well as the optimization procedure is tested by considering results reported by Imgrund et al. [9], in which they showed the feasibility of co-sintering a martensitic (17-4PH) and an austenitic (316L) alloys by varying processing parameters—particularly of the initial particle sizes. To model the densification properties of the alloys (i.e., 17-4PH and 316L), their effective diffusion coefficients at the sintering temperature are first calculated

Table 1 Parameters used in the sintering model

Sintering temperature, T (K)	T_s
Atomic volume, Ω (m^3)	1.18×10^{-29}
Specific surface energy, γ_s (J/m^2)	2.60
Boltzmann constant, k (J/K)	1.38×10^{-23}
Grain growth coefficient, k' (−)	0.50

Table 2 Comparison of model predictions with experimental data for density and initial particle sizes

	Final density (%)		Initial particle size, d50 (μm)	
	Expt	Model	Expt	Model
17-4PH	93.4	96.0	3.51	3.6
316L	96.1	96.0	3.25	3.3

using Thermo-Calc by considering their chemical composition provided in [9]. The evolution of relative density as well as linear shrinkage rates are predicted using the process parameters (green density, temperature, sintering cycle) given in Imgrund et al. [9]. Since the initial particle sizes in [9] are not uniform, the average value from the reported distribution of powder particles is used. Table 1 summarizes the other parameters used in the sintering model.

Table 2 shows the comparison of the final densities in 17-4PH and 316L from the model and experimental measurements after sintering for 1 h at 1300 °C. The model results agree with the experimental observations demonstrating the capability of the model despite the assumptions made on particle size. Figure 4 depicts the evolution of the corresponding sintering rates in both alloys with a wider gap (mismatch) around the middle of the sintering cycle. This shows that stress in the sample (e.g., a tensile stress in the 316L side of the FGM), which is proportional to the mismatch in sintering rates between the two alloys, gradually increases at the middle of the sintering cycle and then decreases and is reversed towards the end of the sintering period.

To show the capability of the optimization approach, the minimization of mismatch in shrinkage rates is performed by minimizing $\Delta(D^s/G^3)$ between 17-4PH and 316L. Note here

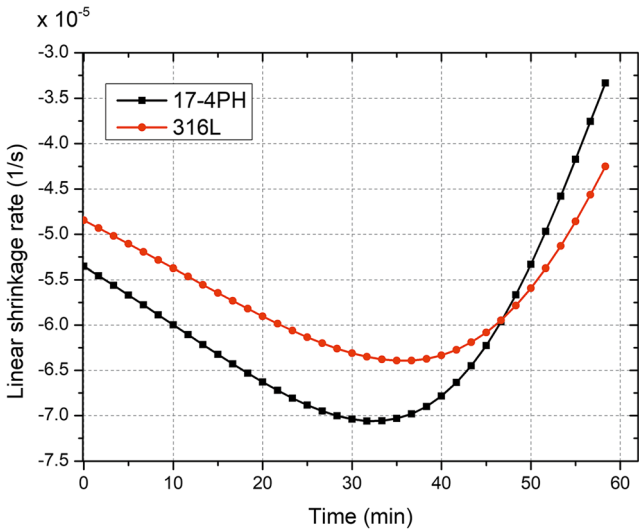

Fig. 4 Model results for the evolution of shrinkage rates in martensitic 17-4PH and austenitic 316L alloys showing the largest mismatch in the middle of the sintering cycle

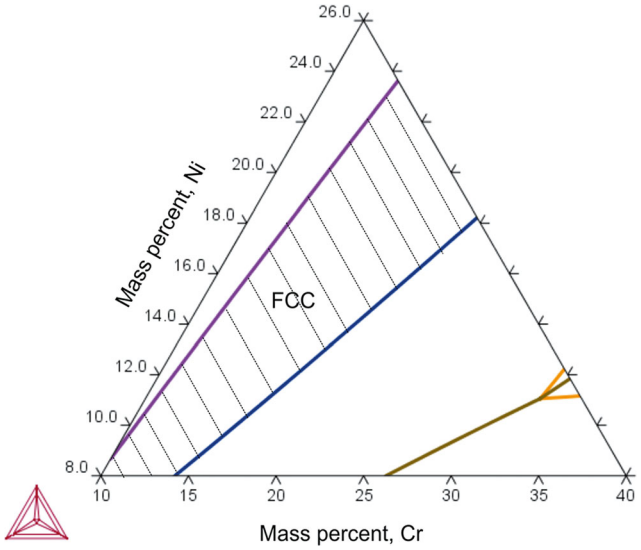

Fig. 5 Isothermal section of Fe-Cr-Ni phase at 1600 K. The shaded section is the FCC region

that the diffusion coefficients are calculated using the standard compositions of 17-4PH and 316L and thus the decision variables during the optimization are the average initial particle sizes. The minimum and maximum bounds for the average initial particle sizes are set to 2 and 10 μm, respectively. After the optimization, the ratio of the initial average particle sizes in 17-4PH and 316L that minimizes mismatch in the sintering rates is determined to be 1.08, see Table 2. By comparison, the corresponding ratio of the average particle sizes reported in [9] for the successful co-sintering of 17-4PH and 316L alloys was 1.09.

The observed agreements between the model and experimental results show that the sintering model (i.e., the main

Table 3 Composition bound of alloying elements (% wt) and initial particle sizes (μm)

Element	Ferritic steel		Austenitic steel		430L	316L
	Min	Max	Min	Max		
Fe	Bal	Bal	Bal	Bal	Bal	Bal
Cr	12	28	11	25	17.0	17
Ni	–	–	8	15	–	12
Cu	–	–	0	3	–	–
Mo	–	–	1	4	–	2.5
Mn	0	4	0	3	1.00	1
C	0	0.06	–	0.03 (fixed)	0.05	0.03
Si	0.50	2.50	–	0.95 (fixed)	1.00	0.75
N	–	–	–	0.10 (fixed)	–	0.10
P	–	–	–	0.04 (fixed)	–	0.04
S	–	–	–	0.03 (fixed)	–	0.03
Particle size	5	15	5	15	–	–

sub-model in the design framework) as well as the optimization approach can reasonably describe experimental observations that resulted in a successful co-sintering of 17-4PH and 316L.

Bounds for Decision Variables

The compositional bounds of the alloying elements for an FGM system defined in "Design Objectives for a Stepwise FGM Structure" are determined using the isothermal section of phase diagram of the constituent alloys at the sintering temperature. Figure 5 shows an isothermal section for an austenitic steel at 1600 K as a function of chromium (Cr) and nickel (Ni) concentration. The compositional bounds for Cr and Ni are thus determined using the extreme limits of the area where the fully austenitic (FCC) phase exists at the required sintering temperature. A similar approach is also used in the case of the ferritic (BCC) alloy. This is done to improve the computational efficiency of the search algorithm by limiting the decision variables to a valid microstructural region.

Table 3 shows the compositional bounds considered in this study for both ferritic and austenitic stainless steel alloys in the FGM system. The composition for each of the elements and the initial particle sizes are made to vary between the minimum (Min) and maximum (Max) bounds. Composition of the interstitial elements of the austenitic steel alloy are fixed because their influence on the effective diffusion coefficient is very small. For comparison, results from an FGM involving standard compositions of 430L ferritic and 316L austenitic alloys are also considered.

In order to investigate the impact of sintering temperature, design optimizations for the best compositional mix in each alloy are performed at four different sintering temperatures, i.e., 1400, 1500, 1550, and 1600 K. These temperatures are chosen considering the optimal sintering temperature of the individual alloys as discussed in Jamaludin et al. [26].

Results and Discussion

The termination criterion is determined by considering improvements in the objective values with respect to the number of generations. Here, improvements in all the objectives are considered, i.e., the difference in the ratio of the effective self-diffusion coefficient to the cube of particle size for A1/A2, $\Delta(D^s/G^3)$, solid solution hardening, σ_{SSH}, in A2 and corrosion resistance (*PRE*) in A2. Figure 6 shows the decrease in $\Delta(D^s/G^3)$ together with improvement in σ_{SSH} as a function of the number of generations during the optimization. Figure 6 also shows a decrease of the difference in the effective diffusion coefficients for A1/A2, i.e., ΔD^s, and an increase in *PRE* in A2 with the number of iterations. The improvements in all the objective values become constant after the 100th iteration. Thus, a maximum of 120 iterations was chosen as the stopping criterion, which is equivalent to a computational time of a few days using desktop computers.

The results in Fig. 6 are obtained after considering the initial population size of $N_p = 2500$. Genetic operations were performed using an encoded binary crossover and a uniform mutation operator. When generating the offspring population,

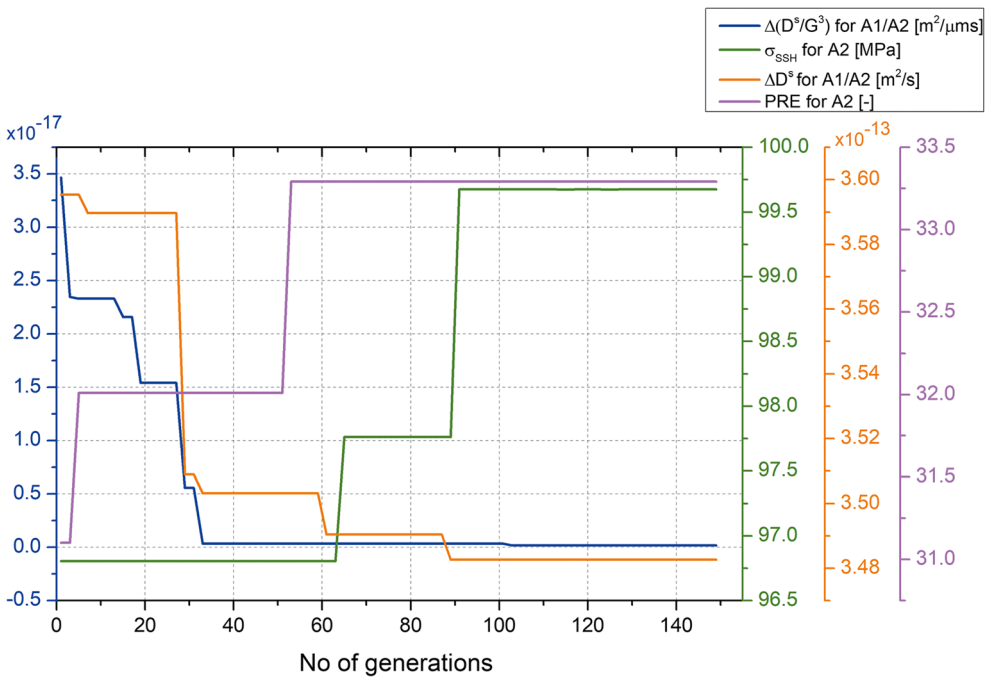

Fig. 6 Improvement of the objective values (maximum or minimum depending on the design goals) as a function of GA iterations or number of generations

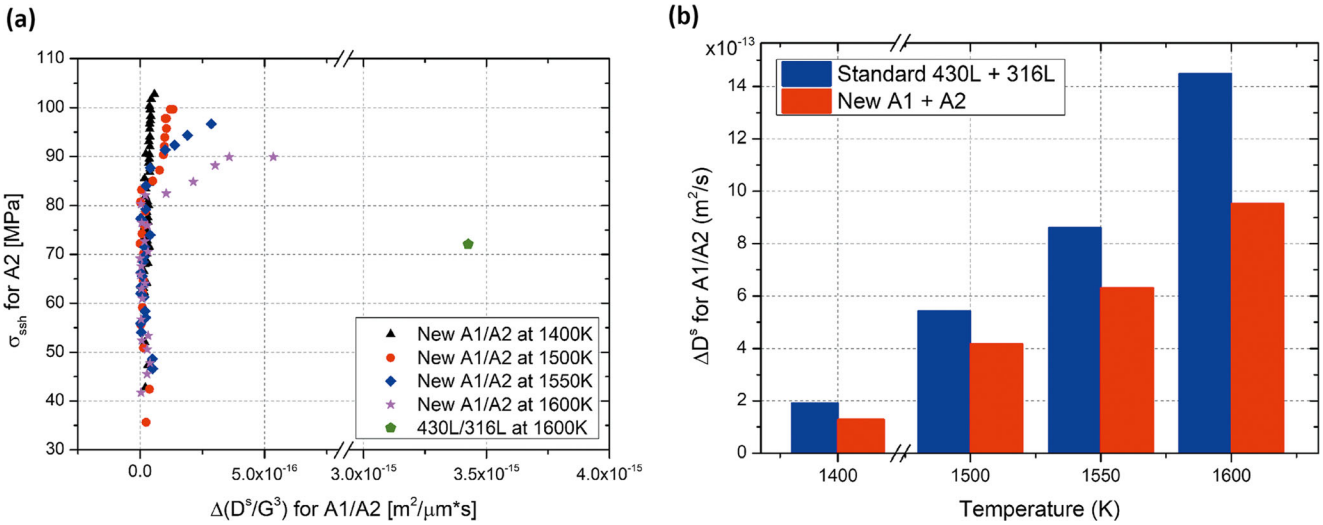

Fig. 7 **a** Pareto-curves for the first versus the second objective values at different sintering temperatures. **b** Comparison of difference in diffusion coefficients at different temperatures

the probability for an individual to serve as a parent, i.e., the crossover probability, was $P_c = 0.7$. The probability for an individual to be mutated was set to $P_m = 0.10$. The mutation operation selects new random values for each gene; these values were uniformly extracted from within the respective lower and upper bounds.

Figure 7 a shows solutions in the Pareto-set considering two objectives, σ_{SSH} for A2 versus $\Delta(D^s/G^3)$ for A1/A2, at four sintering temperatures. A point in each of the Pareto-frontiers corresponds to optimal solutions of the design variables for the pair of alloys in the FGM corresponding to the sintering temperature. Note that all the points in the Pareto-frontier for a given temperature are optimal in the sense that it is impossible to improve one objective without making the other worse. Thus, the choice of the "best" point from the Pareto-set depends on the users' priority. For instance, on the Pareto-frontier corresponding to 1600 K, the solution with the maximum hardness in A2 will have relatively larger mismatch in sintering rates between A1 and A2. The single best point will thus be determined based on the users' priority from hardness in A2 or co-sinterability between A1 and A2.

As shown in Fig. 7 a, higher strengths can be obtained with a decrease in the sintering temperature. This means a reduced value of $\Delta(D^s/G^3)$ for A1/A2, and a higher σ_{SSH}value for A2 can be achieved at lower sintering temperature. For the sake of comparison, a result obtained by considering an FGM produced from the standard ferritic 430L and austenitic 316L alloys at 1600 K is also shown in Fig. 7 a. Comparison of results from the standard alloys with those on the Pareto-frontier shows that it is possible to minimize the mismatch in sintering rates between A1/A2 and simultaneously increase the hardness in A2 by designing a new set of alloys for the FGM.

By choosing a solution (from each of the Pareto-frontiers) with the minimum $\Delta(D^s/G^3)$, it is possible to calculate the difference in the diffusion coefficients, ΔD^s, for A1/A2 in the FGM. Figure 7 b shows a comparison of the ΔD^s for the standard 430L/316L and new A1/A2 at four sintering temperatures. The result shows that by designing new alloy compositions, it is possible to minimize the difference in diffusion coefficients between the alloys in the FGM.

The ΔD^s for A1/A2 decreases with decreasing sintering temperature, demonstrating that co-firing FGMs at lower temperatures can reduce the mismatch in sintering rates between the two alloys and hence avoid defects during 2C-MIM. However, it should be noted that lower temperatures could also affect the optimal sintering behavior in each of the individual alloys resulting in longer dwell times and consequently larger particle growth. Thus, it is necessary to make a trade-off between the optimal sintering temperature of the individual alloys and the suitable co-firing temperature.

Table 4 provides the optimal compositions of the ferritic and austenitic alloys that give the minimum

Table 4 Optimal compositions of the ferritic and austenitic alloys that gives the minimum $\Delta(D^s/G^3)$ at 1600 K

Layer	Cr	Ni	Cu	Mo	Mn	Si	C
Ferritic	25.1	–	–	–	1.20	0.87	0.03
Austenitic	17.57	14.83	1.55	2.7	2.13	0.75	0.03

Table 5 Optimal diffusion coefficients and initial particle sizes for the optimal alloys with the minimum $\Delta(D^s/G^3)$ at different temperatures

Temperature (K)	Diffusion coeff. (m^2/s)		Initial particle sizes (μm)	
	D_1^s	D_2^s	G_1	G_2
1400	1.35×10^{-13}	4.95×10^{-15}	14.25	5.73
1500	4.39×10^{-13}	1.96×10^{-14}	14.45	6.32
1550	6.73×10^{-13}	3.96×10^{-14}	14.33	5.66
1600	1.03×10^{-12}	7.51×10^{-14}	13.38	5.75

mismatch in sintering rates, i.e., $\Delta(D^s/G^3)$ at 1600 K. Comparison of these compositions with the corresponding standard alloys, i.e., 430L and 316L provided in Table 3, shows that a higher amount of Cr and Mn in the ferritic, and higher amount of Ni and Cu in the austenitic alloys is necessary for successful co-sintering of the two alloys.

To clarify the improvements that can be achieved by designing a new set of alloys for FGMs, the shrinkage rates between a combination of standard 430L/316L and new A1/A2 alloys are compared under similar sintering conditions. For this purpose, a solution is chosen (from each of the Pareto-frontiers) with the minimum $\Delta(D^s/G^3)$. The diffusion coefficients as well as the optimal combination of the average initial particle sizes are summarized in Table 5.

Given the diffusion coefficients and average initial particle sizes, the sintering model discussed in "Modeling the Free Sintering Rate" can be used to calculate the evolution in shrinkage rates during a defined sintering cycle. Figure 8 a shows the linear shrinkage rates during isothermal sintering at 1600 K for 130 min. The initial particle sizes and the green density used were 13 μm and 80%, respectively. The 316L alloy sinters very slowly compared to the 430L alloy because the diffusion coefficient in austenitic FCC phase is much lower than in the ferritic BCC phase. Thus, there will be higher stress at the beginning of the co-firing cycle of these two alloys because of the large mismatch in shrinkage rates. This is consistent with experimental observations during co-firing of multi-layers [27].

The linear shrinkage rates for optimal ferritic (A1) and austenitic (A2) alloys are also shown in Fig. 8 a. Calculation of the sintering rates considers the effective self-diffusion coefficients as well as the initial particle sizes for each of the alloys as per the optimization results at 1600 K. The initial green density in each alloy is assumed to be 80%. It is shown that the shrinkage rates in both alloys evolves in a similar manner, resulting in a reduced mismatch in sintering rate as

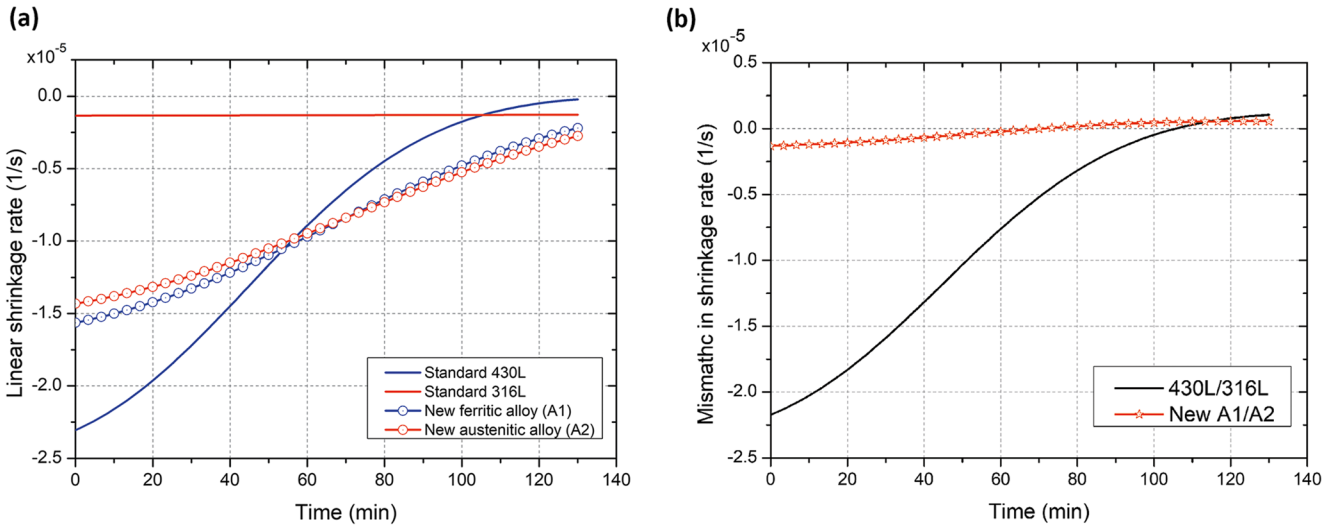

Fig. 8 Comparison of **a** linear shrinkage rates at 1600 K between standard alloys of 430L/316L as well as the new ferritic (A1) /austenitic (A2). **b** Mismatch in shrinkage rates for standard as well as new alloys

shown in Fig. 8 b. These improvements will help reduce the differential stresses and hence processing defect formation during sintering of the FGM system.

Conclusions

The study suggests a new computational methodology for designing alloy systems for stepwise FGMs with improved co-sintering behavior. The methodology independently optimizes the composition, processing parameters, and the performance properties of each of the alloys in the FGM system. The design methodology can thus be used to (1) determine a new composition for each alloy in the FGM, (2) determine the average initial particle size for green bodies of each of the alloys in the FGM, and (3) investigate the optimal co-firing temperature for the FGM. Emphasis is given to improving manufacturability, i.e., co-sintering, by minimizing mismatch in shrinkage rate between the different alloys making the FGM.

The design methodology is validated by comparing model predictions with experimental results from the literature. The capability of the methodology is demonstrated by designing an FGM combining a ferromagnetic ferritic steel and a non-magnetic austenitic steel with the objectives of (1) minimizing mismatch in shrinkage rate between the two alloys and (2) maximizing solution hardening and corrosion resistance in the austenitic alloy. The design provides a non-dominated set of optimal alloys (Pareto-set) in the FGM. Significant improvement of mismatch in sintering rates between the optimal alloys is shown when compared to an FGM produced from standard ferritic (430L) and austenitic (316L) stainless steel alloys.

The computational design method proposed in this study can be used for the efficient design of FGMs which can be produced by two-color metal injection molding. Processing parameters together with the composition of each component of the FGM are optimized simultaneously and independently in order to enhance manufacturability while maintaining or even improving their functional properties. This will serve to minimize the physical experiments usually required to optimize such material systems. The methodology can also be extended by coupling additional sub-models so that additional properties or microstructural complexity can be incorporated in the design space.

Author Contributions G.B.S. conceived the initial idea, supervised the project, and contributed to writing the manuscript. T.T.M. extended the idea, developed the model, performed simulations, and wrote the manuscript. J.Z.L. provided critical comments and contributed to revisions of the manuscript.

Funding This work was funded by The University of Melbourne.

Compliance with Ethical Standards

Competing Interests The authors declare that they have no competing interests.

References

1. Olson GB (1997) Computational design of hierarchically structured materials. Science 277:1237–1242
2. Pollock TM (2016) Alloy design for aircraft engines. Nat Mater 15: 809–815
3. Deschamps A, Tancret F, Benrabah I-E, De Geuser F, Van Landeghem HP (2018) Combinatorial approaches for the design of metallic alloys. Comptes Rendus Phys 19:737–754
4. Li S, Kattner UR, Campbell CE (2017) A computational framework for material design. Integr. Mater. Manuf. Innov. 6:229–248
5. Molla TT, Liu JZ, Schaffer GB (2018) An ICME framework for design of stainless steel for sintering. Integr Mater Manuf Innov 7: 136–147
6. Heaney DF, Suri P, German RM (2003) Defect-free sintering of two material powder injection molded components part I *Experimental investigations*. J Mater Sci 38:4869–4874
7. Johnson JL, Tan LK, Suri P, German RM (2003) Design guidelines for processing bi-material components via powder-injection molding. JOM. 55:30–34. https://doi.org/10.1007/s11837-003-0172-1
8. Manonukul A, Songkuea S, Moonchaleanporn P, Tange M (2017) Effect of weld line positions on the tensile deformation of two-component metal injection moulding. Int J Miner Metall Mater 24:1384–1393
9. Imgrund P, Rota A, Petzoldt F, Simchi A (2007) Manufacturing of multi-functional micro parts by two-component metal injection moulding. Int J Adv Manuf Technol 33:176–186
10. Simchi A, Rota A, Imgrund P (2006) An investigation on the sintering behavior of 316L and 17-4PH stainless steel powders for graded composites. Mater Sci Eng A 424:282–289
11. Mulser M, Baumann A, Ebert S, Imgrund P, Langer I, Petzoldt F (2014) Materials of high hardness and wear resistance joined to stainless steel by 2C-MIM. Adv Powder Metall & Part Mater 4: 140–148
12. Mulser M, Petzoldt F (2016) Two-component metal injection moulding of Ti-6Al-4V and stainless steel bi-material parts. Key Eng Mater 704:148–154
13. Firouzdor V, Simchi A (2010) Co-sintering of M2/17-4PH powders for fabrication of functional graded composite layers. J Compos Mater 44:417–435
14. Cai PZ, Green DJ, Messing GL (1997) Constrained densification of alumina/zirconia hybrid laminates, 2. Viscoelastic stress computation. J Am Ceram Soc 80:1940–1948
15. Kanters J, Eisele U, Rodel J (2001) Cosintering simulation and experimentation: case study of nanocrystalline zirconia. J Am Ceram Soc 84:2757–2763
16. Frandsen HL, Olevsky E, Molla TT, Esposito V, Bjork R, Pryds N (2013) Modeling sintering of multilayers under influence of gravity. J Am Ceram Soc 96:80–89

17. Molla TT, Frandsen HL, Bjork R, Ni DW, Olevsky E, Pryds N (2013) Modeling kinetics of distortion in porous bi-layered structures. J Eur Ceram Soc 33:1297–1305
18. Olevsky EA (1998) Theory of sintering: from discrete to continuum. Mater Sci Eng R-Reports 23:41–100
19. Perrut M (2015) Thermodynamic modeling by the calphad method and its applications to innovative materials. J AerospaceLab:1–11. https://doi.org/10.1276/212015.AL09.10
20. Rahaman MN (2008) Sintering of ceramics, Taylor and Francis Group, Boca Raton
21. Coble RL (1961) Sintering crystalline solids .1. Intermediate and final state diffusion models. J Appl Phys 32:787
22. German RM (2010) Coarsening in sintering: grain shape distribution, grain size distribution, and grain growth kinetics in solid-pore systems. Crit Rev Solid State Mater Sci 35:263–305
23. Walbrühl M, Linder D, Ågren J, Borgenstam A (2017) Modelling of solid solution strengthening in multicomponent alloys. Mater Sci Eng A 700:301–311
24. McGuire MF (2008) Stainless steels for design engineers. ASM International, Materials Park
25. Shukla PK, Deb K (2007) On finding multiple Pareto-optimal solutions using classical and evolutionary generating methods. Eur J Oper Res 181:1630–1652
26. Jamaludin KR, Muhamad N, Rahman MNA, Amin SYM, Ahmad S, Ibrahim MHI (2009) Sintering Parameter Optimisation of the SS316L metal injection molding (MIM) compacts for final density using Taguchi Method, 3rd South East Asian Tech. Univ Consort Symp:258–262
27. Molla T, Ramachandran D, Esposito V, Ni D, Teocoli F, Olevsky E, Bjork R, Pryds N, Kaiser A, Frandsen H (2015) Constrained sintering of bi-layered tubular structures. J Eur Ceram Soc Ceram Soc 35:941–950